ADVANCED FUNCTIONAL MATERIALS
www.afm-journal.de

Oxygen Doping Enables Tailored Built-In Electric Fields in FeOCl/g-C_3N_4 Heterojunctions for Enhanced Peroxymonosulfate Activation

Ying Zeng, Hong Qin, Fuqi Wu, Jing Gao, Wenyang Li, Jiaqi Li, Shengyi Wu, Piao Xu, Cui Lai,* and Ziwei Wang**

Regulating metal-support interactions enables rational design of catalysts with enhanced performance in Fenton-like oxidation reactions. Here, a novel oxygen-doped, stalactite-like g-C_3N_4 supported FeOCl (FeOCl-OCN) is successfully synthesized. Due to the modulation of O doping to the work function (Φ) of g-C_3N_4 support, a delicate built-in electric field (BIEF) oriented from OCN to FeOCl is constructed. Driven by large work function difference ($\Delta\Phi$ = 3.235 eV), the interfacial charge transfer manipulates electron redistribution to achieve a rearrangement of structural Fe(II)/Fe(III). Based on theoretical calculations and mechanism insight, the interaction between FeOCl and OCN exhibits a stronger binding ability to peroxymonosulfate (PMS) and reduces the energy barriers for *O formation, therefore favoring a higher yield of singlet oxygen ($^1O_2$) and high-valent iron-oxo (Fe(IV)=O)− species. As a result, the FeOCl-OCN/PMS system demonstrates a nonradical-dominated pathway, delivering high activity (k_{obs} = 0.250 min^{-1}), robust tolerance to pH variation and resistance, and excellent stability.

1. Introduction

The Fenton-like process is a powerful technique for wastewater decontamination, in which hazardous organic pollutants can be effectively decomposed by produced oxidizing reactive oxygen species (ROS) such as hydroxyl radicals (•OH) and sulfate radicals ($SO_4^{\bullet-}$).[1–4] Particularly, peroxymonosulfate (PMS, HSO_5^-) is an intensively used oxidant in advanced oxidation processes (AOPs) with multitudinous activation methods.[5–7] PMS-based AOPs not only can produce various radicals with strong oxidation (e.g., $SO_4^{\bullet-}$, E_0 = 2.5–3.1 eV and •OH, E_0 = 1.7–2.8 eV), but also can readily lead to the generation of nonradical oxidative species (e.g., $^1O_2$ and Fe(IV)=O).[8–10] Generally, radicals are susceptible to complicated substances in water, while nonradical oxidative species possess longer lifetimes, higher oxidant utilization efficiency, and stronger resistance to environmental interference, thus persistently and effectively degrading organic pollutants.[11,12] Considering the large consumption and secondary pollution readily caused by homogeneous catalysts (e.g., Co^{2+}, Fe^{2+}, etc.), the development of a heterogeneous catalyst toward a nonradical-species-oriented PMS activation process is quite urgent.

Among multifarious heterogeneous catalysts, transition metal-based catalysts with variable chemical states are considered to be efficient PMS activators. Iron oxychloride (FeOCl), an innovative Fenton-like catalyst characterized by its ternary layered structure and reducible electronic properties, has garnered substantial attention due to its structural Fe species and coordination configuration.[13–16] It was reported that the optimized Fe(III)/Fe(II) redox cycle featured by low energy of Fe—Cl bond and regulable Fe(II)/Fe(III) structure gave rise to excellent catalytic activity and selectivity. For example, Wang et al.[17] reported that K^+ intercalated into FeOCl induced a production of ≈10% reduced high-spin Fe(II), which caused a substantial electronic change of the FeOCl and thus mediated a nonradical pathway for H_2O_2 activation with Fe(IV)=O as active species. Recently, Chen et al.[13] reported that the polar surface (i.e., (020) facet) of FeOCl structure can be highly hydrated with H_2O molecules, which drove abundant electrons from unsaturated Fe atoms to

Y. Zeng, H. Qin, F. Wu, J. Gao, W. Li, J. Li, S. Wu, P. Xu, C. Lai
College of Environmental Science and Engineering
Hunan University
Changsha 410082, P.R. China
E-mail: piaoxu@hnu.edu.cn; laicui@hnu.edu.cn
Y. Zeng, H. Qin, F. Wu, J. Gao, W. Li, J. Li, S. Wu, P. Xu, C. Lai
Key Laboratory of Environmental Biology and Pollution Control
Ministry of Education
Hunan University
Changsha 410082, P. R. China
Z. Wang
Department of Applied Physics
The Hong Kong Polytechnic University
Kowloon 999077, China
E-mail: ziweiwang@polyu.edu.hk

The ORCID identification number(s) for the author(s) of this article can be found under https://doi.org/10.1002/adfm.202423664

DOI: 10.1002/adfm.202423664

PDS oxidant. To achieve high efficiency and high selectivity for production ROS, the rational design of unsaturated Fe atoms in the layered structure of FeOCl is a prerequisite for subsequent surface reactions.

The metal-support interface can modulate the electronic structure of surface-bound metal atoms through intricate electronic interactions.[18] Theoretically, the heterostructure interface can induce a redistribution of local electrons, leading to the formation of a directional built-in electric field (BIEF).[19–22] Crucially, the work function, a fundamental surface property of a material defined as the minimum energy required to remove an electron from the Fermi level to the vacuum level, is tunable for the construction of the strong and stable BIEF.[23,24] For example, Zhai et al.[24] tuned the valence state of cobalt oxide (CoO_x) to obtain a Pt@CoO_x electrocatalyst with large $\Delta\Phi$, which showed 4.5-fold higher mass activity than 20% Pt/C by optimizing hydrogen and hydroxide adsorption. In view of this, manipulating BIEF by an elaborately tailored support to induce electrons flow to the FeOCl will theoretically benefit an increased charge density and may contribute to the rearrangement of Fe(II)/Fe(III) (i.e., Fe(III)-to-Fe(II) reduction). Currently, the application of FeOCl-based materials in PMS activation has attracted considerable attention, yet the underlying mechanisms responsible for the selective production of active species through interface modulation remain to be elucidated.

In this work, graphitic carbon nitride (g-C_3N_4) with controllable structure and synthesis, was chosen as a carrier for FeOCl loading. Given that heteroatom-doped (N, P, S, O, etc.) has been proved to definitely affect the strong metal-support interaction,[25–27] the oxygen was doped into g-C_3N_4 support for $\Delta\Phi$ regulation. First, the impact of interfacial interaction and electronic structure alternation of catalysts have been uncovered by characterization, catalytical removal of sulfamethazine (SMZ, a common antibiotic), and the generation of active species. Then, the reasonable catalytic mechanism of PMS activation by FeOCl-OCN was investigated through experiments and density functional theory (DFT) calculations. Finally, the environmental applicability of the FeOCl-OCN /PMS system was overall assessed in multiple conditions. It is expected that this work will enrich the design idea of FeOCl-based catalysts, and pave the way for rapid water purification.

2. Results and Discussion

2.1. Structure and Property

The preparation protocol of OCN-FeOCl is briefly outlined in **Figure 1**a. Previous studies have reported that the incorporation of O heteroatoms could modulate the electronic structure, resulting in the formation of unpaired electrons.[28] Inspired by this, O atoms were doped into the pristine g-C_3N_4 skeleton using cyanuric acid as precursors for the formation of O-doped g-C_3N_4 (OCN). As shown in Figure S1 (Supporting Information), OCN with preferentially exposed (100) and (002) facets were synthesized, with the characteristic peaks at 13.0° and 27.7°.[29] Typically, part of doped O atoms in OCN bonded with sp^2-configurated C atoms to form C═O species (289.0 eV, 3.99%) (Figure S2 and Table S2, Supporting Information), leading to increased O-containing groups. Meanwhile, N atoms in the triazine rings might be substituted by O atoms to form C—O/C═O, along with the decrease in C—N═C in N 1s spectra with the incorporation of cyanuric acid. Notably, OCN featured a porous and hollow structure with lots of pores of varied size, and even extended to form stalactite-like structures (Figure 1b), whereas the CN (without O-doping) presented sheet-like and block-like forms (Figure S3b,c, Supporting Information). This could be attributed to the release of gases (NH_3, CO_2, etc.) during the thermal condensation process, thus destructing the lamellar structure of g-C_3N_4.[30] In this regard, O-doping combined with the fabrication of stalactite-like morphology leads to a massive generation of edges and abundant active sites, which will favor the mass transportation of metals or reactants access to the catalyst.

Importantly, the EPR spectrum also showed that OCN displayed a significantly strengthened signal compared with CN, suggesting a higher concentration of unpaired electrons (Figure S4, Supporting Information). These unpaired electrons provide a stronger covalent metal-support interaction, thus efficiently anchoring metal atoms.[27] A series of OCN with different FeOCl content was thus synthesized by directly heating the mixture of $FeCl_3 \bullet 6H_2O$ and OCN. In theory, when heating to 250 °C, $FeCl_3 \bullet 6H_2O$ would be evaporated and hydrolyzed to form FeOCl ($FeCl_3 \bullet nH_2O \rightarrow FeCl_3 \bullet H_2O + (n\text{-}1)\ H_2O \rightarrow FeOCl + 2HCl$), and the evaporated $FeCl_3$ could also react with the crystalline water and triggered to the formation of FeOCl sheets ($FeCl_3 + H_2O \rightarrow FeOCl + 2HCl$).[18] In addition, functional groups in OCN served as anchoring sites to facilitate the complexation or bonding of metals with oxygen atoms via electrostatic force.[31] As a result, the lamellar-structured FeOCl nanosheets (≈8.9 nm) were widely dispersed on the surface of OCN support or embedded within its porous framework (Figures S3 and S5, Supporting Information; Figure 1d–f). HAADF-STEM EDS-mapping images (Figure 1g) clearly showed the rich distribution of the C and N elements, and Fe, O, and Cl species were centrally distributed in similar locations, indicating the formation of FeOCl. The scattered O element around FeOCl sheets was indexed to the doped oxygen in OCN. HR-TEM images uncovered obvious lattice fringes with a length of ≈0.258 nm (Figure 1f), referring to the (021) crystal plane of FeOCl. As revealed by the XRD patterns, the formation of FeOCl-OCN with a large number of exposed (021) facets was proved, showing a distinct diffraction peak at 35.6°, which was ascribed to (021) crystal plane of FeOCl (Figure S1, Supporting Information). Additionally, all as-prepared FeOCl-OCN displayed similar diffraction patterns to those of parent OCN support and presented gradually increased diffractions in FeOCl loading lifting samples with negligible impacts on OCN support, which was also confirmed by FTIR analysis (Figure S6 and Text S7, Supporting Information).

The surface chemical states and chemical composition of as prepared catalysts were uncovered by X-ray Photoelectron Spectroscopy (XPS). As displayed in **Figure 2**a, the Fe 2p spectra displayed typical $2p_{1/2}$ and $2p_{3/2}$ peaks at 710.4 and 723.6 eV in FeOCl, which corresponded to Fe(II) species. Meanwhile, peaks at a binding energy of 725.4 and 711.7 eV corresponding to Fe(III) species were found. Generally, a shift toward lower energy leads to a charge transfer from the support to the metal, while an upshift represents a reverse charge transfer. Of note, the main peaks of Fe 2p shifted to a lower energy level (709.5 eV, $\Delta \approx 0.9$ eV) compared to pristine FeOCl, and the relative content of Fe(II)

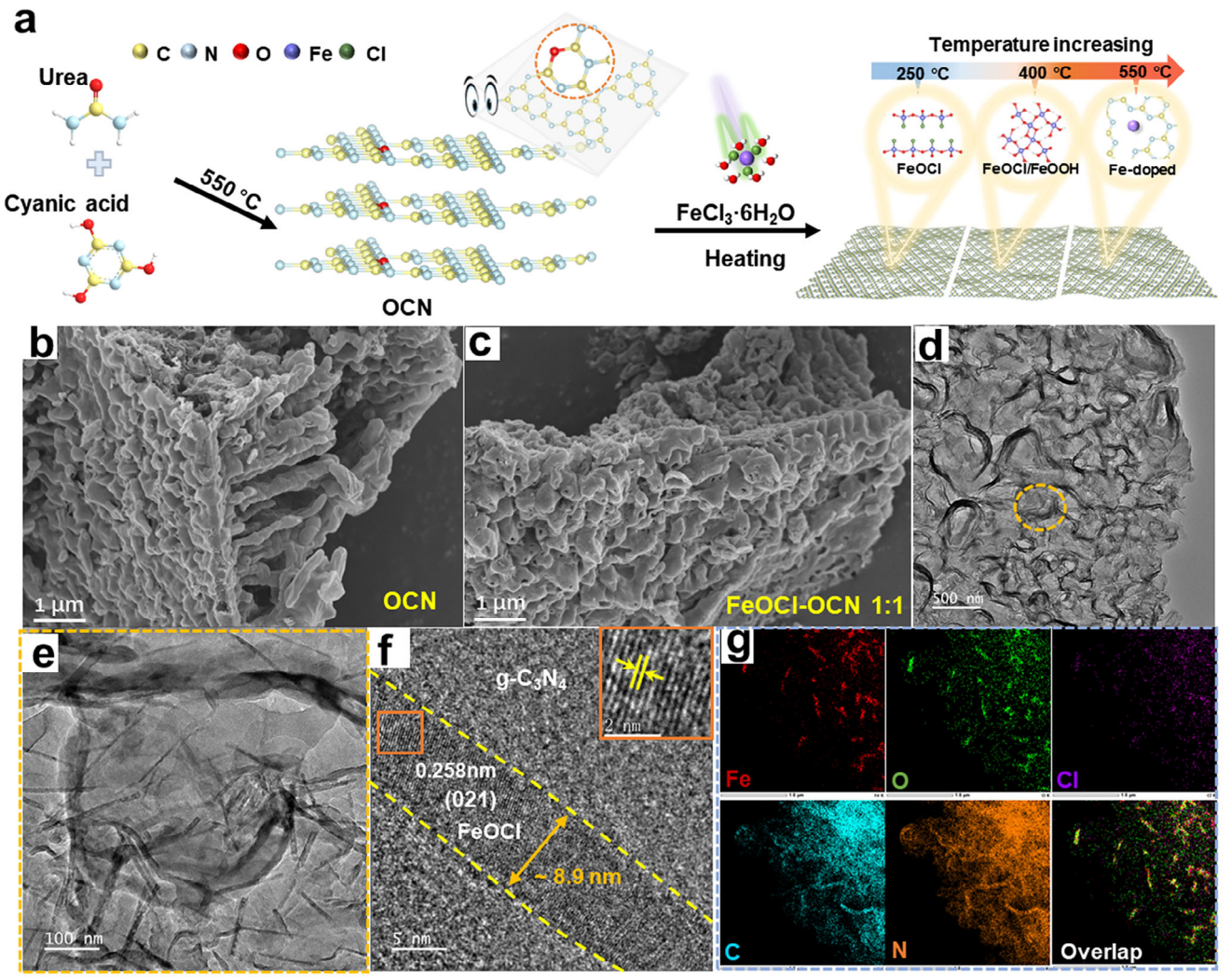

Figure 1. a) Schematic diagram of the preparation of FeOCl-OCN. b,c) SEM of (b) OCN and (c) FeOCl-OCN. d) TEM images and e) the enlarged TEM images of FeOCl-OCN. f) HR-TEM images and g) EDS elemental mapping data of FeOCl-OCN.

obviously increased to 57.2% in FeOCl-OCN (48.2% estimated in FeOCl samples). Correspondingly, a noticeable negative shift was also observed in O 1s and Cl 2p XPS spectra (Figure 2b,c), which collectively indicated that FeOCl had a tendency to gain electrons from OCN, thus leading to partial reduction of Fe(III).[32] It should be mentioned that the Fe 2p spectra of FeOCl-CN presented similar fitting peaks, but showed less downshift, in which the location of Fe(II) $2p_{3/2}$ was negatively shifted by ≈0.3 eV with a 4.6% increase of Fe(II) content. Hence, it can be speculated that a strong interaction exists between FeOCl and OCN, which may arouse an electron migration from OCN to FeOCl, and further favors Fe rearrangement in FeOCl.

Thereafter, DFT calculations were applied to investigate the interfacial electron transfer between FeOCl and OCN (Figure S7, Supporting Information). The work function (Φ) of FeOCl and OCN was determined to be 6.998 and 3.763 eV, respectively (Figure 2d; Table S3, Supporting Information). As such, once the two contact, significant charge transfer might take place automatically from OCN to FeOCl, until reaching Fermi level equilibrium, which was consistent with XPS results. While, the work function of CN was calculated to be higher than OCN (E_{WF} = 4.554 eV), implying that CN possessed higher electron stability and a lower charge transfer to FeOCl. Further, electrochemical tests indicated that FeOCl-OCN possessed lower electrochemical impedance and higher current density (Figure 2e,f). These findings first indicate that a strong interaction between OCN and FeOCl has led to the migration of electrons from OCN to FeOCl, therefore contributing to forming a directional BIEF in FeOCl-OCN. Furthermore, it supports that the Φ of g-C_3N_4 has been favorably tailored by O doping, enabling FeOCl-OCN to exhibit more efficient electron transfer at the coherent heterointerface driven by a large ΔΦ (3.235 eV). Particularly, due to the flat layered structure, FeOCl enables most of the atoms to interact with the support, potentially leading to enhanced charge migration. This involves not only localized charge transfer at the interface but also affords a long-range direct charging of the FeOCl outer surface through charge equilibration with the support, thereby contributing to catalysis.

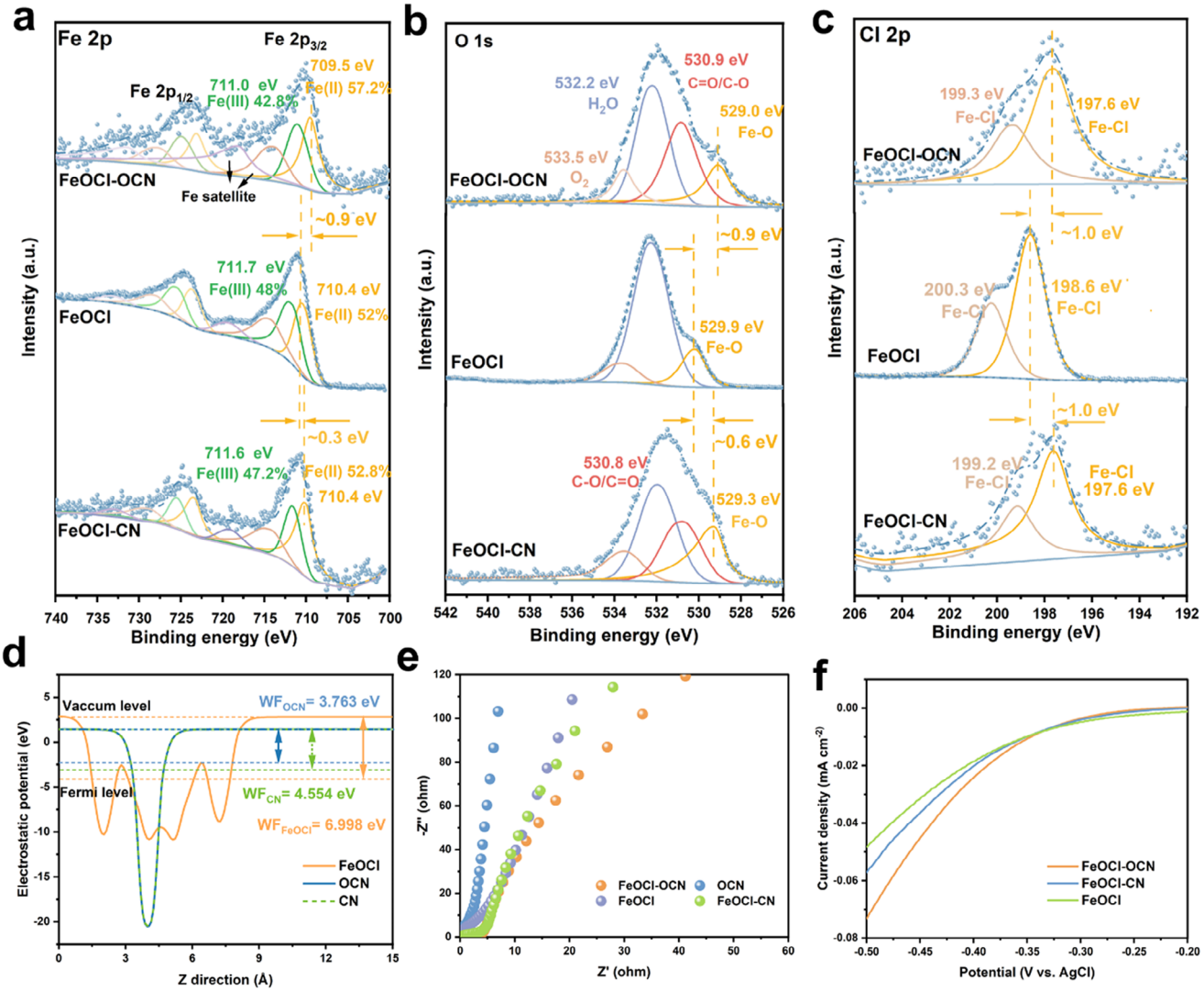

Figure 2. a–c) The high-resolution XPS spectra of (a) Fe 2p, b) O 1s, and c) Cl 2p. d) Work function of FeOCl, OCN, and CN. e) Electrochemical impedance spectroscopy (EIS) Nyquist plots and f) Linear sweep voltammetry (LSV) curves of different samples.

2.2. Fenton-Like Catalytic Performance

The catalytic activation of all catalysts on PMS was examined by the oxidative elimination of SMZ (**Figure 3a**). FeOCl-OCN composites with porous structure showed negligible adsorption for SMZ in 90 min (Figures S8 and S9, Text S8, and Table S4, Supporting Information), and only 22.5% of SMZ was removed by PMS alone in 30 min. Impressively, when FeOCl-OCN was introduced, SMZ was completely degraded with a 52.2% mineralization rate (Figure S10, Supporting Information), achieving the highest reaction rate constant by FeOCl-OCN 1:1 (k_{obs} = 0.250 min^{-1}), which was 19.2 and 7.9 times higher than that of pristine FeOCl and FeOCl-CN, respectively. The performance did not improve at higher loading levels, which was attributed to FeOCl agglomeration (Figure S11, Supporting Information). Notably, FeOCl-OCN 1:5, even at a low loading level, still outperformed the original FeOCl, underlining the critical effect of the BIEF of FeOCl-OCN in PMS activation. The inferior catalytic performance of FeOCl-OCN-400 and FeOCl-OCN-550 also demonstrated this. FeOCl was transformed into FeOOH and doped-Fe at 400 and 550 °C with decreased crystallinity. The FeOOH was reported by 2 orders of magnitude lower •OH generation rate and had a lower work function (4.83 eV) than FeOCl,[14,33] thus weakening and even destructing the BIEF.

Moreover, due to the encapsulation and anchoring effect of OCN, FeOCl-OCN exhibited good stability and reusability in the oxidation process. The leaching amount of Fe ions in the FeOCl-OCN/PMS system (0.27 mg L^{-1}) was much lower than that in the FeOCl/PMS system (2.79 mg L^{-1}) and kept below 0.62 mg L^{-1} under different pH conditions (Figure S12, Supporting Information). Also, leached Cl ions were detected and showed a noticeable discrepancy compared to leached Fe ions, likely due to the weak Fe−Cl bond energy in FeOCl.[34] The released Cl^- could take part in PMS activation as well as cause more coordination of unsaturated Fe sites for PMS activation. In the cyclic experiment, FeOCl-OCN 1:1 achieved over 95% degradation rate after

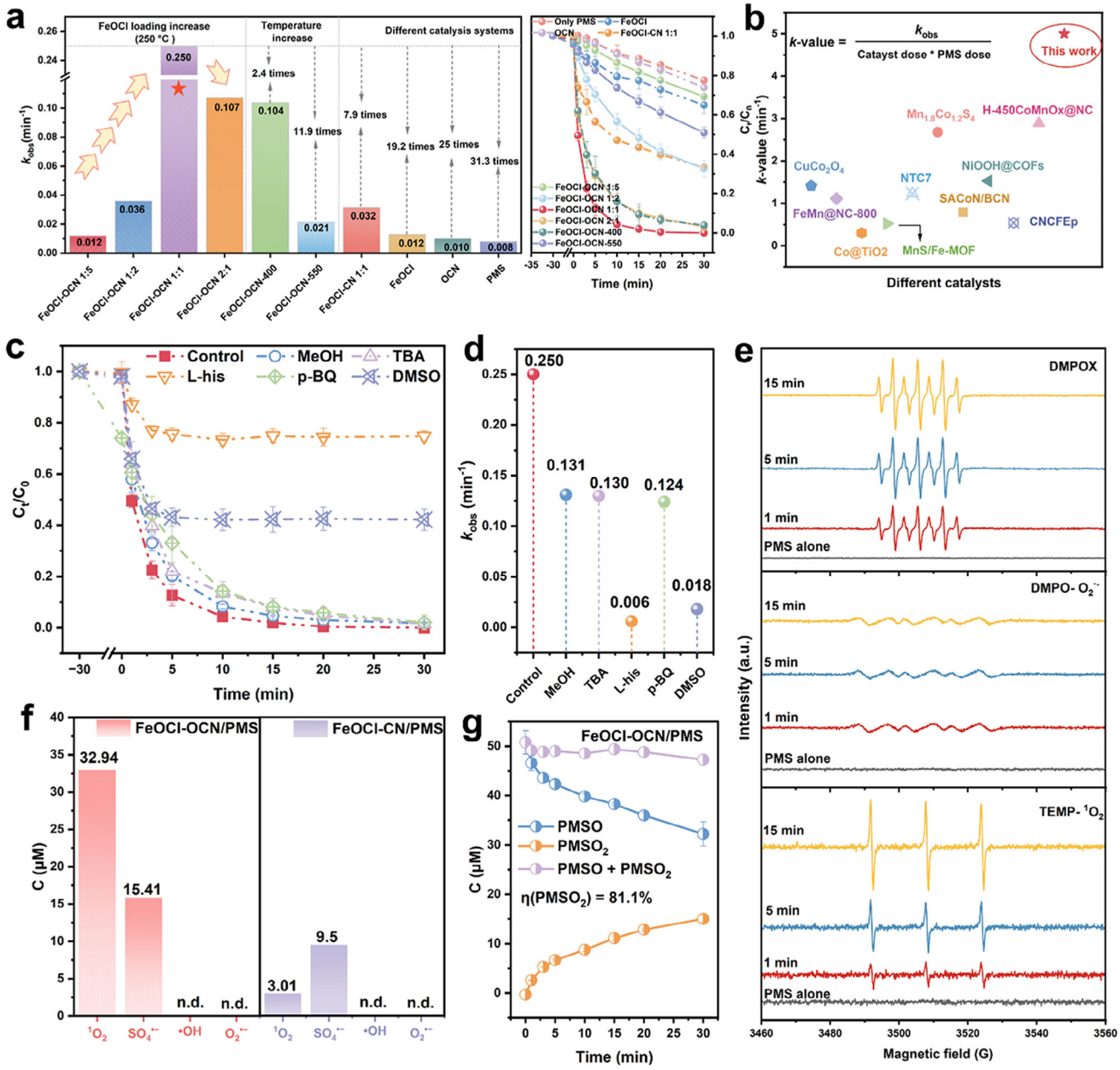

Figure 3. a) The catalytic performance of different catalysts. b) A comparison between FeOCl-OCN and other reported catalysts for SMZ removal. c) Effects of various scavengers on SMZ degradation. d) The reaction rate constants of SMZ in the presence of different scavengers. e) EPR spectra for the detection of DMPOX, DMPO-$O_2^{\bullet-}$, and TEMP-$^1O_2$ in the FeOCl-OCN/PMS system. f) The quantitative analyses of ROS in different catalytic systems. g) Removal of PMSO and formation of $PMSO_2$ in FeOCl-OCN/PMS system. Reaction conditions: [SMZ] = 10 mg L^{-1}, [PMS] = 0.25 mM, [catalysts] = 0.2 g L^{-1}, T = 25 °C, [initial pH] = 5.80.

three repeated uses with invisible structural variation (Figures S13 and S14, Supporting Information). It is worth mentioning that the FeOCl-OCN 1:1/PMS system also outperforms most recently reported catalysts (Figure 3b; Table S5, Supporting Information). Based on the above results, FeOCl-OCN 1:1 (abbreviated to FeOCl-OCN) was used in the following experiments, and the influence of operating parameters on SMZ removal was investigated, with results presented in Text S9 and Figure S15 (Supporting Information)

2.3. Identification of Reactive Species

Active species in the PMS-AOP system are generally divided into radicals and nonradicals. Herein, scavenging experiments, EPR analysis, and probe experiments were conducted to reveal the reactive species in FeOCl-OCN/PMS systems. Radicals, such as $SO_4^{\bullet-}$, •OH, and $O_2^{\bullet-}$ were examined using methyl alcohol (MeOH), tert-butanol (TBA), and *p*-benzoquinone (*p*-BQ) as scavengers, respectively. The results showed that different

concentrations of those radical scavengers could hardly influence the removal of SMZ (Figure 3c,d; Figure S16a–c, Supporting Information), without obvious EPR signals of those radicals (Figure 3e). It is of note that the trapping agent of DMPO was directly oxidized into DMPOX instead of forming DMPO-•OH/$SO_4^{\bullet-}$ adduct (Figure 3e), indicating a featured nonradical oxidation regime occurring on the catalyst surface.[35] Probe experiments further indicated that •OH and $O_2^{\bullet-}$ were hardly yielded in FeOCl-OCN/PMS systems, but ≈15.41 µM of $SO_4^{\bullet-}$ was produced (Figure 3f; Figures S17–S19, Supporting Information). The small amount of $SO_4^{\bullet-}$ explained the phenomenon that MeOH and TBA resulted in a slight decrease of k_{obs} but didn't affect SMZ removal. In brief, these results collectively demonstrated the negligible effect of $SO_4^{\bullet-}$, •OH, and $O_2^{\bullet-}$ in FeOCl-OCN/PMS system.

However, it was obvious that SMZ degradation was severely suppressed by L-histidine (L-his) and DMSO, which served as scavengers for $^1O_2$ and high-valent metals, respectively (Figure 3a,b; Figure S16d,e, Supporting Information). Typically, SMZ degradation was severely suppressed after L-his addition, and the k_{obs} was inhibited to 0.006 min^{-1}. Visually, TEMP-trapped EPR spectra showed that FeOCl-OCN exhibited strong $^1O_2$ signal intensity (Figure 3e), and even markedly enhanced when replacing H_2O solvent with D_2O (Figure S20, Supporting Information), suggesting the generation of $^1O_2$. Hence, we further tested the possible generation of $^1O_2$ using a 9,10-diphenylanthracene (DPA) probe ($k = 1.3 \times 10^6$ M^{-1} s^{-1}). The highest $^1O_2$ concentration at 32.94 µM was trapped in the case of FeOCl-OCN/PMS after 30 min, which was ≈11 times higher than that in FeOCl-CN/PMS system (Figure 3f; Figure S21, Supporting Information). This demonstrated that FeOCl-OCN was more conducive to ceaselessly activating PMS to form $^1O_2$, and also supported the direct oxidation of DMPO discussed before.

The pathways of $^1O_2$ production in the FeOCl-OCN/PMS system were further investigated. The influence of PMS self-decomposition and the interaction of PMS and dissolved oxygen (DO) were excluded via a series of experiments (Figure S22, Supporting Information; Figure 3e). Therefore, we speculate that $^1O_2$ presumably originates from the interaction of PMS on active sites. In this pathway, Fe atoms on the polar surface of FeOCl might act as active centers in FeOCl-mediated Fenton-like catalysis. For this reason, chelating agents for transition metals, including oxalate, Ethylene Diamine Tetraacetic Acid (EDTA), and sodium thiocyanate (NaSCN) were selected as inhibitors of iron sites. As shown in Figure S23 (Supporting Information), oxalate (100 mM) suppressed the SMZ removal to 65%, indicating the vital role of iron sites. Notably, an almost block in SMZ degradation occurred in the presence of 1–2 mM NaSCN, reconfirming the primary contribution of Fe centers to the reaction. Likewise, NaSCN greatly suppressed the signal intensity of $^1O_2$, directly validating that the Fe sites motivated $^1O_2$ generation (Figure S24, Supporting Information). Meanwhile, low amounts of leached Fe ions were detected during the whole reaction in the FeOCl-OCN/PMS system, and ignorable roles in SMZ degradation were confirmed via homogeneous degradation at leached Fe levels, suggesting that the primary reaction took place on the unsaturated iron atoms over the catalyst surfaces (Figure S25, Supporting Information). Theoretically, FeOCl consists of distorted edge-sharing $FeCl_2O_4$ octahedra, with tunable Fe–Cl bonds and reducible electronic structure, which can favor_the rearrangement of Fe(III)/Fe(II). For example, an almost 25% Fe^{3+} tansformation to Fe^{2+} was characterized by intercalating guests into FeOCl, and the rate of •OH generation driven by Fe^{2+} was 3–4 orders of magnitude higher than that driven by Fe^{3+}.[36] In our present study, an obvious increase of Fe(II) was found in FeOCl-OCN compared to FeOCl-CN (57.2% vs 52.8%, Figure 2a), primarily attributed to a charge-transfer process between FeOCl and OCN driven by the substantial ΔΦ. Benefiting from these, the generation of $SO_4^{\bullet-}$ and $^1O_2$ over FeOCl-OCN was 1.67 and 11 times higher, respectively, than that over FeOCl-CN (Figure 3f).

The variable valence and regulable coordination structure of FeOCl on OCN can facilitate consecutive two-electron transfer, inspiring the generation of high-valent iron-oxo species (e.g., Fe(IV/V)═O), which could also oxidize organic pollutants with a redox potential of ≈1.80 V. As shown in Figure 3g, the selective transformation of methyl phenyl sulfoxide (PMSO) to methyl phenyl sulfone ($PMSO_2$) was calculated at a conversion rate of ≈81% ($\eta = \Delta[PMSO_2]/\Delta[PMSO]$), based on the result that ≈18.54 µM PMSO was consumed along with 15.04 µM of $PMSO_2$ generation. Noticed that ≈4.52 µM PMSO was oxidized by PMS, producing 4.29 µM $PMSO_2$ in the pure PMS system (Figure S26, Supporting Information). With this regard, η in FeOCl-OCN/PMS system was corrected to ≈77%, suggesting the yield of high-valent metal-oxo species driven by FeOCl-OCN. Meanwhile, the removal of SMZ was inhibited to 58% with the reaction rate decelerated to 0.018 min^{-1} at 40 mM DMSO dosage (Figure S16e, Supporting Information; Figure 3b). Subsequently, the derivation of high-valent iron-oxo species was explored. The XPS analysis further demonstrated that the relative portion of Fe(II) markedly decreased to 51.9% (Δ = 5.3%) corresponding to the increased Fe(III) content after the reaction (Figure S27, Supporting Information), illustrating that Fe(II) rather than Fe(III) might be accountable for the Fe(IV)═O generation. The increased Fe(III) content could derive from Fe(IV)═O through the consumption of pollutants, or one-electron self-decay when the substrate was absent. Furthermore, in the presence of DMSO, the peak intensity of TEMP-$^1O_2$ was weakened, suggesting the possible roles of Fe(IV)═O in $^1O_2$ generation (Figure S28, Supporting Information).[37] Inspired by this, the rearranged Fe(III)/Fe(II) structure has been implicated in the generation of high-valent metal species and $^1O_2$ during SMZ oxidation.

2.4. Mechanisms of Reactive Species Generation

A generally accepted point is that the formation and decomposition of the catalyst-PMS* complex was the trigger step of the heterogeneous Fenton reaction. LSV showed that a significant current density increased with PMS addition, suggesting that metastable PMS complexes (FeOCl-OCN-PMS*) were formed via direct interaction between the PMS and FeOCl-OCN. An apparent variation after the addition of SMZ further confirmed the electron transfer between SMZ and this metastable FeOCl-OCN-PMS* complexes. Hence, the adsorption process of PMS to form catalyst-PMS* complex is regarded as the initiation step.

As presented in **Figure 4b**, the adsorption energies of PMS on FeOCl-OCN and FeOCl-CN were calculated to be −2.11 and −1.36 eV, respectively. The stronger PMS adsorption capacity of

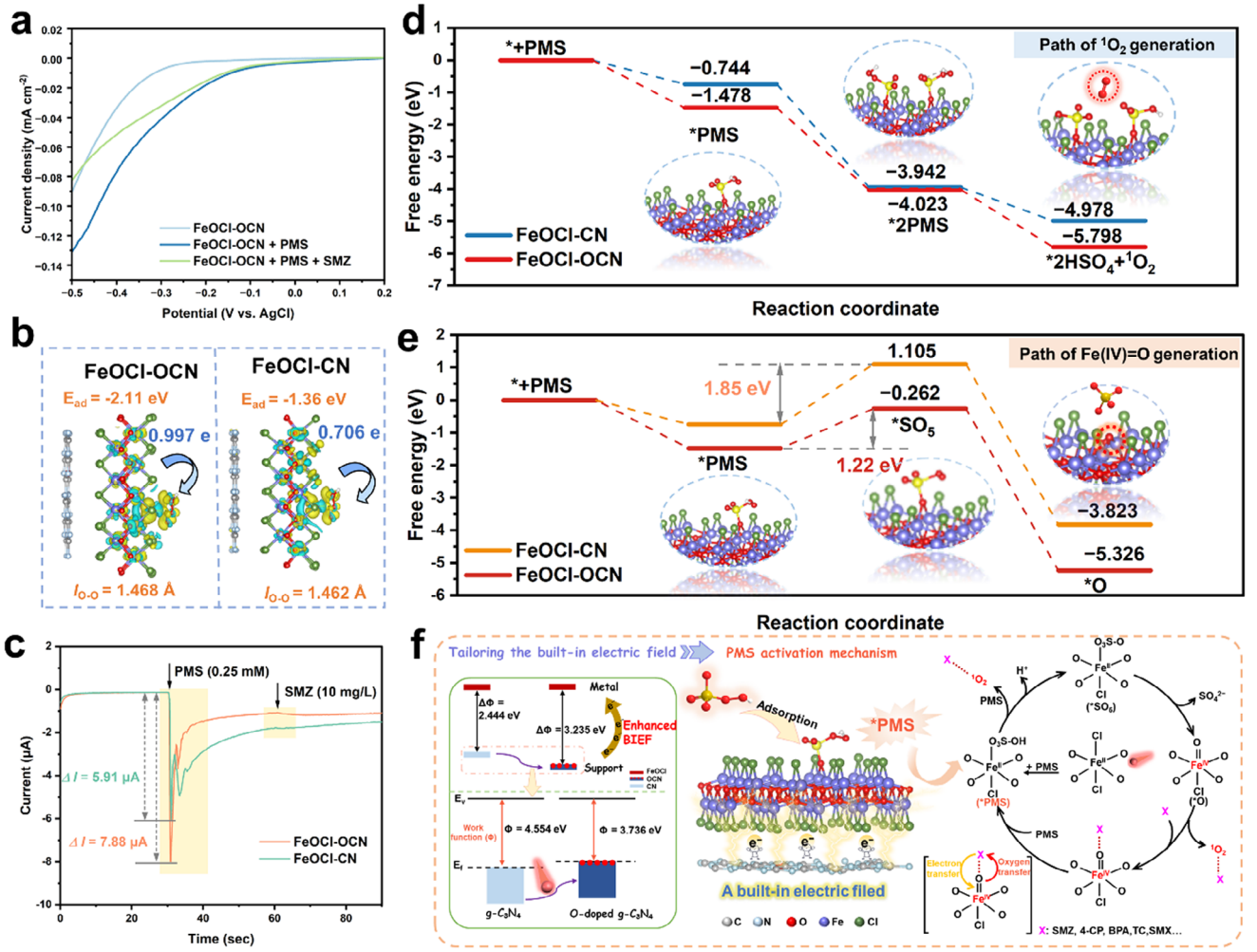

Figure 4. a) The LSV curves of FeOCl-OCN in different conditions. b) PMS adsorption energy, length of the O–O bond, charge density difference diagrams, and Bader charges on FeOCl-OCN and FeOCl-CN. c) i–t curves of different electrodes. d,e) The free energy profiles of (d) $^1O_2$ and (e) Fe(IV)=O in different systems. f) The schematic illustration of $^1O_2$ and Fe(IV)=O production on FeOCl-OCN by PMS activation.

FeOCl-OCN than FeOCl-CN implied that oxygen doping is beneficial for PMS adsorption, consistent with their variation in work function (Figure 2d). Regarding the interfacial electron transfer discussed above, the chronoamperometry (i-t) tests were conducted, and results showed that PMS injection provoked a dramatical current increase at ΔI = 7.88 μA in FeOCl-OCN/PMS, which was more significant than FeOCl-CN/PMS system (ΔI = 5.91 μA) (Figure 4c). Most importantly, the electron transfer number from FeOCl-OCN to PMS was ≈0.997 |e|, based on charge density difference and Bader charge analysis, while ≈0.706 |e| transferred from FeOCl-CN to PMS (Figure 4b). The higher electron transfer indicated the effective charge accumulation and chemisorption property between PMS and FeOCl-OCN, liable to the formation of FeOCl-OCN-PMS* complex.[38] DFT calculations further reaffirmed that *PMS was initially formed through chemically bonding to active Fe sites on FeOCl-OCN, with a free energy of −1.478 eV (vs −0.744 eV for FeOCl-CN) (Figure 4d), suggesting the higher affinity of Fe sites on FeOCl-OCN. The above results collectively reveal that oxygen doping plays a dual function, which enhances interfacial charge transport capacity and ultimately improves the formation of FeOCl-OCN-PMS* complex, and even FeOCl-OCN-2PMS* complex.

DFT calculations were employed to elucidate the potential pathway for the selective production of $^1O_2$ and Fe(IV)=O. Theoretically, $^1O_2$ and Fe(IV)=O are usually triggered by O–H or O–O bond cleavage in PMS, in which *O is the key intermediate.[8,10] According to previous studies, O_β in PMS might accept one electron from O_α with the generation of SO_4^{2-} ($H-O_\alpha-O_\beta-SO_3^-$ → $H^+ + O_\alpha + {}^-O_\beta-SO_3^-$), whereas electron loss and proton release occurred for O_α, and then further reacted with another O_α on the adjacent site in PMS for $^1O_2$ generation ($:O_\alpha + :O_\alpha$ (on the adjacent site) → $^1O_2$).[39] With this regard, the reaction energy of O–O bond cleavage pathway for $^1O_2$ generation was calculated, by considering the interaction of two oxygen atoms from two adsorbed PMS molecules on Fe sites (*2PMS) for $^1O_2$ production ($\equiv HSO_5^- + \equiv HSO_5^- \rightarrow 2HSO_4^- + {}^1O_2$).[38] Evidently, an exothermic course for the generation of FeOCl-OCN-2PMS* (−3.942 eV) was calculated (Figure 4d), suggesting that the reaction process in this pathway was thermodynamically favored. What's clear is that the cleavage of O–O bonds is a crucial

prerequisite to produce $^1O_2$. Fortunately, an elongated O–O bond length of PMS (1.468 Å, Figure 4b) was observed on FeOCl-OCN (vs 1.462 Å on FeOCl-CN), which facilitated bond dissociation to form active species. In this pathway, two O atoms from *2PMS reacted to yield $^1O_2$ and desorbed into solution, with the lowest free energy over FeOCl-OCN (−5.798 eV), marking the great spontaneity of this reaction. Of note, FeOCl-OCN showed improved adsorption ability for each intermediate, accounting for a higher yield of $^1O_2$ in the FeOCl-OCN/PMS system than that in FeOCl-CN/PMS. Finally, the remaining $*HSO_4$ would release protons to form SO_4^{2-} ($2HSO_5^- \rightarrow 2H^+ + 2SO_4^{2-} + {}^1O_2$). The sharply declined pH value of the solution after adding PMS directly supported a coupled proton release process occurring during SMZ degradation (Figure S29, Supporting Information).

As the self-decay of Fe(IV)=O will occur in water, the Fe(IV)=O generation is also driven by FeOCl-OCN-PMS*. Previous studies demonstrated that catalyst-PMS* could behave like an anode, with its surface potential increasing by the accumulation of *PMS, thus enabling direct oxidation of Fe species in the catalyst.[40] In our study, *PMS and 2*PMS formation on rearranged Fe sites are both energetically favorable. Through DFT calculation, the breaking of O–H bonds in *PMS first occurred to generate $*SO_5$ (−0.262 eV), with proton releasing to the solution (Figure 4d). Then, the heterolytic cleavage of the O–O bond in $*SO_5$ finally led to *O (i.e., Fe(IV)=O) formation after a two-electron transfer and O-atom transfer (−5.326 eV). Most importantly, the rearranged Fe(II)/Fe(III) configuration might sustain the localization of electrons on dispersed Fe(II) sites, endowing an isolated environment (akin to that in oxygenases P450 and zeolite) to maintain their high valence states.[14,17] Notably, although the rate-determining step of *PMS to $*SO_5$ is thermodynamically unfavorable,[38,41] the FeOCl-OCN/PMS system exhibited a significantly reduced energy barrier (from 1.437 to 1.22 eV) compared to FeOCl-CN/PMS system, indicating that the production of *O also benefitted by this tailored BIEF. It is worth mentioning that *O as a key intermediate could also participate in $^1O_2$ generation as discussed above ($*O + *O \rightarrow {}^1O_2$),[41] which accounted for the decreased TEMP-$^1O_2$ signal with DMSO addition (Figure S28, Supporting Information).

Combining experimental and theoretical studies, the possible catalytic mechanism of FeOCl-OCN for PMS activation was proposed (Figure 4f). First, PMS was adsorbed on catalysts and quickly formed FeOCl-OCN-PMS* complexes, acting as a reaction trigger. Due to the strong BIEF, the charge will transfer from electron-rich Fe sites to the electron-deficient O–O bond PMS, leading to the O–O and O–H bonds cleavage. For one thing, the interaction between two O atoms from two adsorbed *2PMS results in the yield of $^1O_2$, releasing a remarkable energy of 5.798 eV. For another, the accumulated FeOCl-OCN-PMS* species propel the oxidation of Fe(II) in FeOCl. *O is produced via a two-electron and O-atom transfer process, with H–O and O–O bonds cleavage, and it can be well-maintained owing to a favorable Fe coordination environment. The energy barrier for *O species (1.22 eV) was found significantly decreased by O-doping modulation. Subsequently, $^1O_2$ will be desorbed to nearby or diffuse to bulk solution to attack pollutants, fulfilling degradation and even mineralization. While, Fe(IV)=O confined over the catalyst surface will oxidize the adsorbed substrates through an O-atom transfer reaction and then release the oxygenated product, with Fe(IV)=O reduced to Fe(III)/Fe(II) for regenerated catalytic sites. Besides, part of Fe(IV)=O would involve $^1O_2$ generation through the interaction of *O intermediates. Ultimately, the constructed strong BIEF will improve the redox cycle in the Fe center, thus accelerating Fe(II)/Fe(III)/Fe(IV) cycle to continuously produce $^1O_2$ and Fe(IV)=O for oxidative degradation of multiple contaminants.

2.5. Applicability in Environment

Given the merits of nonradicals ($^1O_2$ and Fe(IV)=O) which could dodge interference from multiple substances, the application potential of the FeOCl-OCN/PMS system was evaluated in different water matrices. First, all of the typical inorganic ions and natural organic matter (e.g., humic acid (HA)) did not affect the removal rate of SMZ by FeOCl-OCN, only with slight inhibition by the presence of HCO_3^- (**Figure 5**a; Figure S30, Supporting Information). This was because the pH value increased to alkaline (5.8 to 8.31–8.60) after adding HCO_3^- (Table S6, Supporting Information), which had an adverse effect on the reaction (Text S9, Supporting Information). Intriguingly, the degradation efficiency was dramatically enhanced with the addition of Cl^-, and especially, SMZ was rapidly eliminated within 3 min at 100 mM level (Figure 5b). As previous studies reported, reactive halogens (e.g., Cl_2/HClO) with strong oxidation capacity could be produced through PMS oxidation.[42,43] Here, NH_4^+ as a quencher for HClO[44] sharply decreased the k_{obs} of FeOCl-OCN/PMS/Cl^- (Figure S31, Supporting Information), demonstrating the involvement of Cl_2/HClO in SMZ removal. Considering the low Cl^- leaching in the FeOCl-OCN/PMS system, the contribution of Cl_2/HClO could be ignored. Further, degradation experiments were conducted in actual waters (Xiangjiang River, Taozi Lake, Hou Lake, and tap water). Despite the adverse pH range values of these actual water, measured at 7.97, 8.80, 8.73, and 8.59 respectively, satisfactory oxidation efficiency was still achieved with SMZ removal rate of over 96% (Figure 5c). The degradation intermediates of SMZ in the FeOCl-OCN/PMS system were ultimately determined by HPLC/MS. It was evidenced that $^1O_2$ and Fe(IV)=O species effectively degraded SMZ with the main degradation pathway of bond cleavage (N–S/S–C/N–C), oxidation, ring open and desulfurization process (Figures S32 and S33 and Text S10, Supporting Information). The biotoxicity of SMZ and the transformed products was predicted by the Ecological Structure–Activity Relationship (ECOSAR) class program. The results suggested that the acute toxicity and chronic toxicity of various intermediates were much lower than SMZ (Figure 5d). Hence, the FeOCl-OCN/PMS system not only has effective oxidation ability but also possesses good environmental safety.

Additionally, the selectivity of the FeOCl-OCN-/PMS catalysis was verified by degrading a diverse array of pollutants. As reported, nonradicals could act as an electrophilic agent, enabling the selective degradation of electron-rich pollutants.[11] As illustrated in Figure 5e, FeOCl-OCN-/PMS system, armed with $^1O_2$ and Fe(IV)=O species, rapidly degraded electron-rich pollutants such as sulfamethoxazole (SMX), 4-chlorophenol (4-CP), phenol, tetracycline (TC), and bisphenol A (BPA), with k_{obs} of 0.121, 0.616, 0.355, 0.432, and 0.227 min^{-1}, respectively. In contrast,

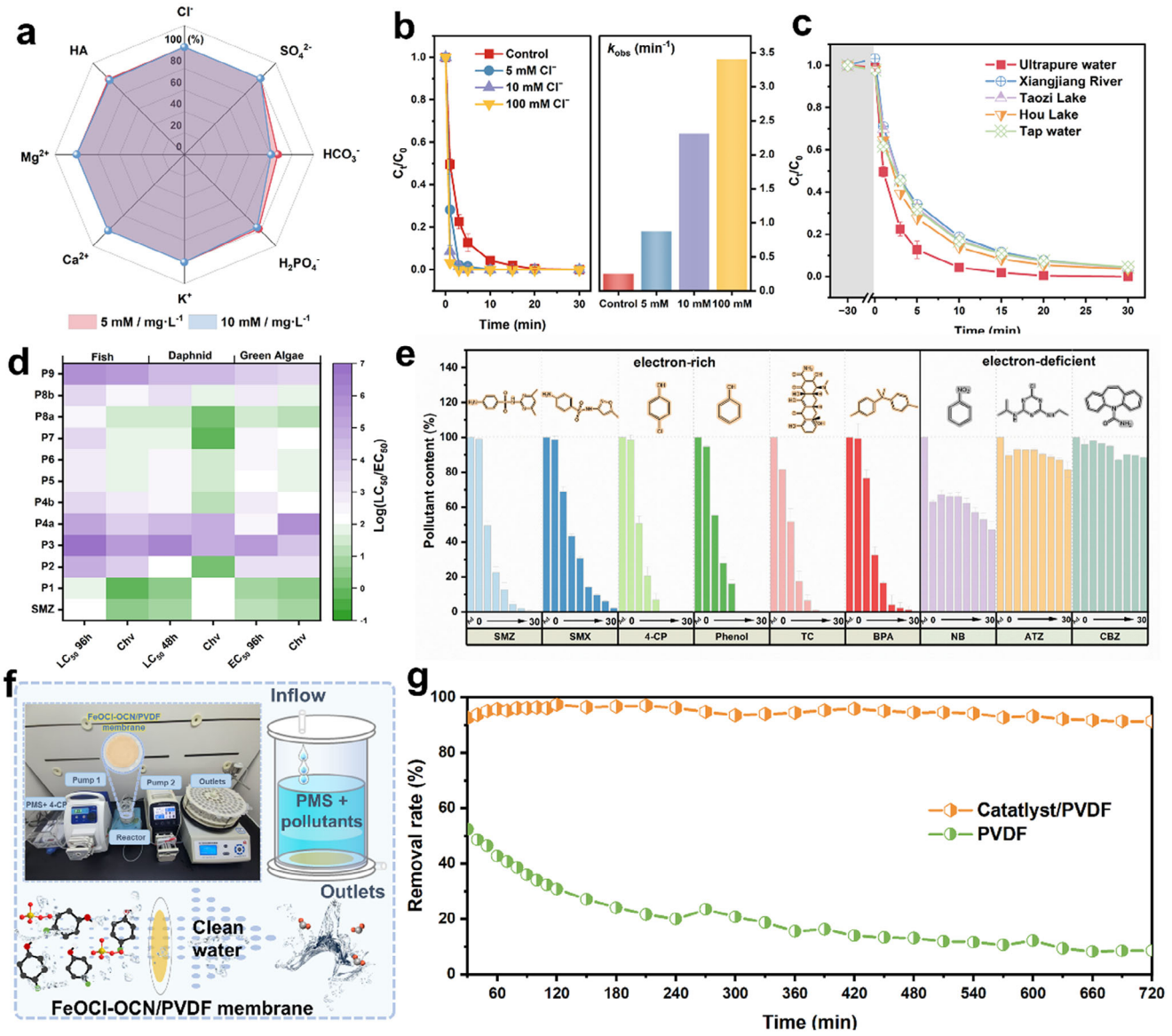

Figure 5. a) Effect of various anions, cations, and HA on SMZ degradation. b) The performance of FeOCl-OCN/PMS system with an injection of chloride ion. c) Influence of actual water on SMZ degradation in FeOCl-OCN/PMS system. d) The estimated acute and chronic toxicity of the SMZ and transformation products. e) Degradation of different pollutants in the FeOCl-OCN/PMS system. f) Device to simulate the practical application of the flow system. g) 4-CP removal in the flow system. Reaction conditions: [SMZ] = 10 mg L^{-1}, [PMS] = 0.25 mM, [catalysts] = 0.2 g L^{-1}, T = 25 °C, [initial pH] = 5.8, [flow rate] = 0.5 mL min^{-1}.

electron-deficient pollutants such as nitrobenzene (NB), atrazine (ATZ), and carbamazepine (CBZ) exhibited prohibitively low degradation efficiency, evidenced by k_{obs} of 0.012 min^{-1}, 0.004 min^{-1}, and 0.003 min^{-1}, respectively. From this, a long-term run experiment with 4-CP as the model pollutant was implemented for further verification (Figure 5f). Inspiringly, 91–98% degradation was achieved during a 720 min continuous run by passing through a FeOCl-OCN/PVDF membrane (Figure 5g). The total leakage of Fe ions during the reaction was below 0.03 mg L^{-1} (Figure S34, Supporting Information). Overall, the above results collectively underscored the environmental applicability of the FeOCl-OCN/PMS system, highlighting the superiority of the nonradical pathway of this Fenton-like system.

3. Conclusion

This work prepared an oxygen-doped stalactite-like g-C_3N_4 supported FeOCl catalyst (FeOCl-OCN) as a highly efficient PMS activator for wastewater treatment. The oxygen doping facilitated an enhanced BIEF from the g-C_3N_4 substrate's interlayer to the surface of FeOCl, promoting rapid and extensive interfacial electron migration. This electron accumulation at the heterointerface drove the rearrangement of Fe(II)/Fe(III), which exhibits favorable characteristics for PMS activation. Through experimental verification and DFT calculations, FeOCl-OCN showed strong adsorption capacity for PMS molecules and reduced the energy barrier for key reaction intermediates of *O production.

Consequently, FeOCl-OCN presented a nonradical dominated pathway for PMS activation, showing higher selectivity for the generation of $^1O_2$ and Fe(IV)=O species than FeOCl-CN/PMS system, resulting in efficient degradation of various pollutants. Benefitting from these, the FeOCl-OCN/PMS system exhibited strong resistance to various interference and robust stability, underscoring the promising practical applications of FeOCl-OCN in wastewater treatment.

4. Experimental Section

Reagents and Characterization: The information on the used chemicals and reagents was presented in Text S1 (Supporting Information). Details of the characterization methods were described in Text S2 (Supporting Information). The analytical methods, calculation formulas, and DFT calculations were recorded in Texts S3–S6 and Table S1 (Supporting Information).

Synthesis of Catalysts—Synthesis of O-Doped g-C_3N_4: The 20 g urea and 10 g cyanic acid were used as precursors for O-doped g-C_3N_4 (OCN) synthesis,[30] which were first mixed by mechanical ball milling process in a planetary ball milling apparatus. Then, the mixtures were sealed in a ceramic crucible and heated in a muffle furnace at 550 °C (2.3 °C min^{-1}) for 180 min. The obtained solids were thoroughly washed with deionized (DI) water and dried at 60 °C (12 h) for further use. For comparison, the pristine g-C_3N_4 (CN) was prepared using urea as a precursor under the same conditions.

Synthesis of Catalysts—Synthesis of FeOCl/g-C_3N_4: FeOCl/g-C_3N_4 composites were obtained by a two-step method of impregnation and calcination. Specifically, a certain amount of $FeCl_3 \bullet 6H_2O$ and OCN powder were dispersed in acetone solution and the well-distributed suspension was formed through stirring and sonication. With the slow evaporation of acetone at ambient temperature, Fe(III) precursors were sucked into the holes of the OCN matrix owing to the capillary force,[45] and the Fe-OCN solids were obtained subsequently. By heating the Fe-OCN mixture to 250 °C for 60 min, FeOCl/g-C_3N_4 composites were finally synthesized under an argon atmosphere (FeOCl-OCN). The products were washed with DI water and acetone to remove residual $FeCl_3$ and dried overnight at 60 °C. Through adjusting the mass ratio of $FeCl_3 \bullet 6H_2O$ and OCN powder (1:5, 1:2, 1:1, 2:1), a series of catalysts were prepared, labeled as FeOCl-OCN 1:5, FeOCl-OCN 1:2, FeOCl-OCN 1:1, FeOCl-OCN 2:1. The Fe loading amount of as-obtained FeOCl-OCN composites was 2.07%, 3.51%, 3.82%, and 7.91%, respectively. The FeOCl transformation on OCN was also explored by increasing temperature to 400 °C and 550 °C. For comparison, the pristine FeOCl was synthesized by heating $FeCl_3 \bullet 6H_2O$ at similar conditions, and the FeOCl-CN samples were synthesized in the same way by replacing OCN with CN.

Experimental Procedures: Batch experiments were performed in a 100 mL glass beaker under magnetic stirring at 25 °C. The catalytic activity of the catalysts was evaluated by the abatement of SMZ. The catalysts at desired amounts with SMZ solution were first stirred for 30 min to achieve the adsorption-desorption equilibrium, and reactions were initiated by adding PMS. The initial pH of the SMZ solutions used was 5.80 and was not adjusted unless stated. At set intervals, 1 mL samples of the reaction solution were withdrawn and passed through a 0.22 µm filter membrane, with excess sodium sulfite to stop the reaction for subsequent analysis.

Supporting Information

Supporting Information is available from the Wiley Online Library or from the author.

Acknowledgements

This work was supported by the National Natural Science Foundation of China (52070077, U20A20323), the National Program for Support of Top–Notch Young Professionals of China (2014), the Program for Changjiang Scholars and Innovative Research Team in University (IRT-13R17), the Hunan Provincial Science and Technology Plan Project (2022JJ20013, 2021JJ40098), and the Science and Technology Innovation Program of Hunan Province (2022RC1121), the Fundamental Research Funds for the Central Universities (531118010226).

Conflict of Interest

The authors declare no conflict of interest.

Data Availability Statement

The data that support the findings of this study are available in the supplementary material of this article.

Keywords

built-in electric field, high-valent metal, oxygen doping, PMS, singlet oxygen

Received: December 3, 2024
Revised: January 6, 2025
Published online: January 20, 2025

[1] B. C. Hodges, E. L. Cates, J. H. Kim, *Nat. Nanotechnol.* **2018**, *13*, 642.
[2] D. B. Miklos, C. Remy, M. Jekel, K. G. Linden, J. E. Drewes, U. Hübner, *Water Res.* **2018**, *139*, 118.
[3] Q. Y. Tian, P. Xu, D. L. Huang, H. Wang, Z. W. Wang, H. Qin, Y. Z. He, R. J. Li, L. S. Yin, S. Chen, Y. Zhao, *J. Environ. Chem. Eng.* **2023**, *11*, 109719.
[4] L. Chen, Z. Y. Zhang, R. Yang, X. J. Wang, J. Y. Yu, H. Jiang, W. J. Zhang, B. D. Xi, X. J. Sun, N. J. Li, *J. Environ. Manage.* **2024**, *369*, 122354.
[5] F. Ghanbari, M. Moradi, *Chem. Eng. J.* **2017**, *310*, 41.
[6] Y. Sun, C. Ma, D. Wu, X. Liu, N. Li, X. Fan, Y. Li, G. Zhang, F. Zhang, W. Peng, *Water Res.* **2023**, *244*, 120542.
[7] X. Li, R. Lv, W. Zhang, M. Li, J. Lu, Y. Ren, Y. Yin, J. Liu, *Water Res.* **2023**, *228*, 119363.
[8] J. Lee, U. von Gunten, J. H. Kim, *Environ. Sci. Technol.* **2020**, *54*, 3064.
[9] Y. He, H. Qin, Z. Wang, H. Wang, Y. Zhu, C. Zhou, Y. Zeng, Y. Li, P. Xu, G. Zeng, *Appl. Catal., B.* **2024**, *340*, 123204.
[10] Y. W. Gao, Z. H. Chen, Y. Zhu, T. Li, C. Hu, *Environ. Sci. Technol.* **2020**, *54*, 1232.
[11] Y. Yan, Z. Wei, X. Duan, M. Long, R. Spinney, D. D. Dionysiou, R. Xiao, P. J. J. Alvarez, *Environ. Sci. Technol.* **2023**, *57*, 12153.
[12] Z. Weng, Y. Lin, S. Guo, X. Zhang, Q. Guo, Y. Luo, X. Ou, J. Ma, Y. Zhou, J. Jiang, B. Han, *Angew. Chem., Int. Ed.* **2023**, *62*, e202310934.
[13] X. Xu, S. Zhang, Y. Wang, Y. Lin, Q. Guan, C. Chen, *Environ. Sci. Technol.* **2023**, *57*, 12922.
[14] X. Yang, X. Xu, J. Xu, Y. Han, *J. Am. Chem. Soc.* **2013**, *135*, 16058.
[15] C. Tan, Q. Xu, T. Sheng, X. Cui, Z. Wu, H. Gao, H. Li, *J. Hazard. Mater.* **2020**, 123084.
[16] Y. M. Zhao, Y. X. Zhao, X. Yu, D. Z. Kong, X. R. Fan, R. Z. Wang, S. J. Luo, D. W. Lu, J. Nan, J. Ma, *Water Res.* **2022**, *220*, 118710.
[17] J. Wang, K.-P. Hou, Y. Wen, H. Liu, H. Wang, K. Chakarawet, M. Gong, X. Yang, *J. Am. Chem. Soc.* **2022**, *144*, 4294.
[18] Y. Zeng, Z. Wang, P. Xu, C. Lai, H. Qin, Y. He, Y. Li, X. Huo, Q. Tian, C. Wang, *Coordin. Chem. Rev.* **2024**, *518*, 216051.
[19] S. Zhang, C. Tan, R. Yan, X. Zou, F.-L. Hu, Y. Mi, C. Yan, S. Zhao, *Angew. Chem., Int. Ed.* **2023**, *62*, 202302795.

[20] H. Xu, J. Li, X. Chu, *Nanoscale Horiz.* **2023**, *8*, 441.
[21] S. Zuo, D. Li, Z. Guan, F. Yang, J. Song, H. Xu, D. Xia, H. Li, X. Li, *Chem. Eng. J.* **2022**, *430*, 133004.
[22] S. Y. Zuo, Y. C. Ding, L. Wu, F. Yang, Z. Y. Guan, S. Ding, D. S. Xia, X. H. Li, D. Y. Li, *Water Res.* **2023**, *231*, 119631.
[23] J. Li, J. Hu, M. Zhang, W. Gou, S. Zhang, Z. Chen, Y. Qu, Y. Ma, *Nat. Commun.* **2021**, *12*, 3502.
[24] L. Zhai, X. She, L. Zhuang, Y. Li, R. Ding, X. Guo, Y. Zhang, Y. Zhu, K. Xu, H. J. Fan, S. P. Lau, *Angew. Chem. Int. Ed. Engl.* **2022**, *61*, 202116057.
[25] F. Herold, T. Imhof, P. Roumeliotis, P. Schühle, M. Ledendecker, M. Ronning, *Carbon* **2023**, *207*, 207.
[26] P. Yin, Q.-Q. Yan, H.-W. Liang, *Angew. Chem., Int. Ed.* **2023**, *62*, 202302819.
[27] Z. Wang, Z. Yi, L. W. Wong, X. Tang, H. Wang, H. Wang, C. Zhou, Y. He, W. Xiong, G. Wang, G. Zeng, J. Zhao, P. Xu, *Adv. Mater.* **2024**, *36*, 2404278.
[28] Y. Meng, Z. F. Li, J. Tan, J. Li, J. X. Wu, T. T. Zhang, X. H. Wang, *Chem. Eng. J.* **2022**, 429.
[29] F. Chen, L. L. Liu, J. H. Wu, X. H. Rui, J. J. Chen, Y. Yu, *Adv. Mater.* **2022**, *34*, 2202891.
[30] X. Wang, C. Zhou, R. Shi, Q. Liu, G. I. N. Waterhouse, L. Wu, C.-H. Tung, T. Zhang, *Nano Res.* **2019**, *12*, 2385.
[31] G. Zhu, W. Zhu, Y. Lou, J. Ma, W. Yao, R. Zong, Y. Zhu, *Nat. Commun.* **2021**, *12*, 4152.
[32] I. C. Gerber, P. Serp, *Chem. Rev.* **2019**, *120*, 1250.
[33] Y. Kang, Z. Mao, Y. Wang, C. Pan, M. Ou, H. Zhang, W. Zeng, X. Ji, *Nat. Commun.* **2022**, *13*, 2425.
[34] S. Zhang, T. Hedtke, Q. Zhu, M. Sun, S. Weon, Y. Zhao, E. Stavitski, M. Elimelech, J.-H. Kim, *Environ. Sci. Technol.* **2021**, *55*, 9266.
[35] Y. Han, C. Zhao, W. Zhang, Z. Liu, Z. Li, F. Han, M. Zhang, F. Xu, W. Zhou, *Appl. Catal., B.* **2024**, *340*, 123224.
[36] I. Jarrige, Y. Q. Cai, S. R. Shieh, H. Ishii, N. Hiraoka, S. Karna, W. H. Li, *Phys. Rev. B.* **2010**, *82*, 165121.
[37] Y. Ding, S. Zuo, D. Li, Z. Guan, F. Yang, *ACS Appl. Mater. Interfaces.* **2023**, *15*, 5058.
[38] L. Zhang, Y. Sun, R. L. Ge, W. H. Zhou, Z. M. Ao, J. H. Wang, *Appl. Catal., B.* **2023**, *339*, 123130.
[39] G. Bi, R. Ding, J. Song, M. Luo, H. Zhang, M. Liu, D. Huang, Y. Mu, *Angew. Chem., Int. Ed.* **2024**, *63*, 202401551.
[40] C. Cheng, W. Ren, F. Miao, X. Chen, X. Chen, H. Zhang, *Angew. Chem., Int. Ed.* **2023**, *62*, 202218510.
[41] P. Z. Yang, Z. H. Cao, Y. H. Long, D. F. Liu, W. L. Huang, S. H. Zhan, M. Li, *Acs Cata* **2023**, *13*, 12414.
[42] G. Lente, J. Kalmár, Z. Baranyai, A. Kun, I. Kék, D. Bajusz, M. Takács, L. Veres, I. Fábián, *Inorg. Chem.* **2009**, *48*, 1763.
[43] L. Lai, J. Yan, J. Li, B. Lai, *Chem. Eng. J.* **2018**, *343*, 676.
[44] L. Chen, X. Zuo, S. Yang, T. Cai, D. Ding, *Chem. Eng. J.* **2019**, *359*, 373.
[45] H. Yang, S. Song, R. Rao, X. Wang, Q. Yu, A. Zhang, *J. Mol. Catal. A. Chem.* **2010**, *323*, 33.